Available online at www.sciencedirect.com

ScienceDirect

Geochimica et Cosmochimica Acta 298 (2021) 55–69

Geochimica et Cosmochimica Acta

www.elsevier.com/locate/gca

Multi-mode magnesium diffusion in sanidine: Applications for geospeedometry in magmatic systems

Hannah I. Shamloo [a,b,*], Christy B. Till [a], Richard L. Hervig [a]

[a] School of Earth and Space Exploration, Arizona State University, Tempe, AZ 85281, United States
[b] Now at College of Earth, Ocean, and Atmospheric Sciences, Oregon State University, Corvallis, OR 97331, United States

Received 29 June 2020; accepted in revised form 28 January 2021; Available online 5 February 2021

Abstract

The duration of magmatic processes can occur over a wide range of time from as long as millennia to as short as hours. It is therefore important to have a variety of geospeedometers that are sensitive to different timescales. The diffusivity of Mg in K-bearing feldspar such as sanidine has previously been a critical gap in the application of geospeedometry, as sanidine is a ubiquitous phase in dacites and rhyolites and also hosts a variety of major and trace elements with variable diffusivities. Here we present the results of a series of 1-atm diffusion experiments in order to constrain the diffusivity of Mg in sanidine. Two compositions of sanidine (Or_{71} and Or_{82}) and crystallographic orientations (*c*-parallel and *c*-perpendicular) are investigated, showing Mg diffusion is isotropic with little to no resolvable major element compositional dependence. Additionally, Mg diffusion in sanidine simultaneously operates by a fast- and slow-path diffusion mechanism as suggested by irregular depth profile shapes that do not conform to an analytical solution to the diffusion equation. Therefore, we employed a model that considers multi-site diffusion reactions in order to determine diffusion coefficients. The following Arrhenius relationships are obtained for Mg diffusion in sanidine:

$D_{Or71\text{-}Fast} = 4.2\ E\text{-}12\ \exp(-275 \pm 14\ kJ\ mol^{-1}/RT)\ m^2\ s^{-1}$,
$D_{Or71\text{-}Slow} = 1.4\ E\text{-}05\ \exp(-369 \pm 15\ kJ\ mol^{-1}/RT)\ m^2\ s^{-1}$,
$D_{Or82\text{-}Fast} = 1.6\ E\text{-}05\ \exp(-283 \pm 14\ kJ\ mol^{-1}/RT)\ m^2\ s^{-1}$,
$D_{Or82\text{-}Slow} = 3.9\ E\text{-}04\ \exp(-405 \pm 15\ kJ\ mol^{-1}/RT)\ m^2\ s^{-1}$.

Fast-path diffusivities for Mg in sanidine are similar to those of Mg in plagioclase determined by Van Orman et al. (2014). Slow-path diffusion in sanidine is at least a few orders of magnitude slower than fast-path diffusion. Slow-path diffusion may be rate-limited by exchange reactions between divalent cations such as Ba and Sr with K, and Mg with Al. Fast-path diffusion likely operates by interstitial and/or vacancy diffusion. Equipped with these new diffusivities, this study calculates timescales for magmatic rejuvenation that likely initiated the Lava Creek Tuff supereruption at Yellowstone Caldera to be as short as weeks but no more than a few decades. This work also demonstrates the complexity that may exist in experimentally-derived geospeedometers and the importance of careful application to natural systems.

Keywords: Multi-mode diffusion; Geospeedometry; Magnesium; Sanidine; Lava Creek Tuff

1. INTRODUCTION

The diffusion of elements in minerals is now recognized as a powerful tool that enables the determination of the rates of natural processes such as the thermal histories of meteorites, or processes that occur in the magma chambers

* Corresponding author at: College of Earth, Ocean, and Atmospheric Sciences, Oregon State University, Corvallis, OR 97331, United States
E-mail address: shamlooh@oregonstate.edu (H.I. Shamloo).

https://doi.org/10.1016/j.gca.2021.01.044
0016-7037/

beneath volcanoes (e.g., Costa and Chakraborty, 2004, Morgan et al., 2006, Martin et al., 2008, Druitt et al., 2012, Saunders et al., 2012, Cooper and Kent, 2014, Chamberlain et al., 2014, Van Orman et al., 2014, Till et al., 2015, Gualda and Sutton, 2016, Rubin et al., 2017). This is due to the major advancements that have been made in the spatial resolution of analytical tools as well as the increasing availability of experimental data in the past few decades. This has allowed for the unprecedented determination of timescales through geospeedometry, also known as diffusion chronometry, that relates the chemical variations in a zoned mineral to time (e.g., Lasaga, 1983, Turner and Costa, 2007, Druitt et al., 2012, Matthews et al., 2012, Chamberlain et al., 2014, Till et al., 2015, Rubin et al., 2017, Shamloo and Till, 2019). For example, numerous studies have relied on a magma's crystal cargo to track its storage conditions prior to eruption, including its temperature, pressure, and chemistry through time (e.g., Morgan et al., 2006, Bindeman and Valley, 2001, Allan et al., 2013, Audétat, 2013, Cashman and Sparks, 2013, Bachmann et al., 2014, Cooper and Kent, 2014, Till et al., 2015, Gualda and Sutton, 2016, Stelten et al., 2017, Shamloo and Till, 2019). Recent work emphasizes the importance of using multiple chronometers in a single mineral phase to make interpretations of a magma's thermal history to avoid errors in excess of thousands of years that can arise from interpreting only a single element-mineral chronometer (e.g., Till et al., 2015, Ruth et al., 2018, Shamloo and Till, 2019). For this reason, it is imperative to develop and use diffusion chronometers within a single crystal phase with diffusivities that vary over orders of magnitude to capture diverse events occurring over short to long timescales.

Feldspar has become an increasingly popular phase for diffusion chronometry due to its abundance in Earth's crust and ubiquity in magmatic environments (e.g., Costa et al., 2003, Morgan et al., 2006, Cooper and Kent 2014, Till et al., 2015). A number of cation diffusion studies have been performed on feldspar (e.g., Grove et al., 1984, Giletti and Shanahan, 1997, Cherniak and Watson, 1992, 1994, Cherniak, 1996, 2002, 2003, 2010, Faak et al., 2013). Mg diffusion in plagioclase, in particular, is relatively fast compared to larger cations such as Ba and Sr in feldspar (e.g., LaTourrette and Wasserburg, 1998, Faak et al., 2013, Van Orman et al., 2014). This is useful for capturing magmatic processes that occur over timescales as short as years to days at magmatic temperatures (e.g., Martin et al., 2008, Saunders et al., 2012, Druitt et al., 2012). More recently, Mg diffusion in plagioclase has been shown to be dependent on major element composition, and increases with increasing albite content (i.e., relative Na content; Van Orman et al., 2014). Increasing diffusivity with albite content is also observed for other cations in plagioclase such as Pb, Sr, Ba, and Nd (Cherniak and Watson, 1992, 1994; Giletti and Casserly, 1994; Cherniak, 1995, 2002).

Sanidine, a variety of alkali feldspar, is a common phase in volcanic systems that produce dacite and rhyolite and contains measurable amounts of Mg (ppm to tens ppm; Till et al., 2015). However, the absolute diffusivity of Mg in sanidine and its dependence on major element chemistry is currently unknown. Elemental partitioning of Ba and Sr (Ren, 2004), as well as Sr diffusion data (Cherniak and Watson, 1992), have been shown to change as a function of the major element composition of sanidine and have proven to be useful chronometers for magmatic studies (Chamberlain et al., 2014, Morgan and Blake, 2006, Till et al., 2015, Shamloo and Till, 2019). To that aim, this study presents the results of 1-atm diffusion experiments to determine Mg diffusivity in sanidine and explore its potential as a diffusion chronometer.

2. METHODS

2.1. Samples and experimental design

Diffusion experiments were performed using natural crystals of sanidine from Eifel, Germany, including one from Rockeskyll Volcanic Complex (Or_{71}) and another from Rieden Volcanic complex (Or_{82}). These crystals were chosen for diffusion experiments because of their homogeneity and lack of exsolution textures as shown by our own analysis and by multiple investigators (Parsons and Lee, 2005 and references therein). Samples were generously provided by both the Mineralogical and Geological Museum at Harvard (MGMH # 112914) and by Jürgen Schreuer at Ruhr Universität Bochum. Each crystal was oriented with respect to *c*-parallel and *c*-perpendicular crystallographic orientations, and cut with a precision diamond wire saw into small $\sim 2 \times 3$ mm rectangular slabs. Crystal slabs were then "mirror" polished on one side with the final polishing step being colloidal silica (0.06 μm). Crystals were then pre-annealed at 1000 °C for 48 hr in air in order to equilibrate point defects of all grains to conditions similar to those experienced during experiments (after Cherniak, 2002). Infrared spectra reveal that Eifel sanidine can contain up to 0.013–0.036 wt% H_2O as a structural constituent in the feldspar M site (Beran, 1986, Lehmann, 1984, Hofmeister and Rossman, 1985). However, we assume the pre-anneal step destabilizes the hydrous species potentially present in Eifel sanidine causing it to diffuse out of the crystal. What remains uncertain is if the hydrous species diffuses via a coupled substitution with another chemical species present in Eifel sanidine. While Yund (1984) suggests that major element (i.e., Na^+ and K^+) diffusion in nominally

Table 1
Average EPMA analyses of Eifel sanidine used as starting material for diffusion experiments.

Wt.%	Eifel Or_{71}	Eifel Or_{82}
SiO_2	64.52	63.96
TiO_2	0.01	0.02
Al_2O_3	18.82	18.63
FeO	0.16	0.16
MnO	0.01	0.00
MgO	0.00	0.00
CaO	0.00	0.00
Na_2O	3.05	1.80
K_2O	12.14	13.90
BaO	1.19	0.97
Total	99.88	99.44

Ca-free feldspars (such as Eifel sanidine, Table 1) seems to be independent of the presence of a hydrous species, our experiments are not buffered for hydrogen fugacity (see experimental details below), and therefore acknowledge the lack of understanding regarding the role H may play in the diffusion of other trace species during these experiments.

The source of Mg used for the diffusion experiments were mixtures of high purity MgO, Al_2O_3, and SiO_2 in 1:1:2 molar proportions that was then mechanically mixed in a 1:6 weight ratio with crushed sanidine from the same crystal the slabs were cut from (similar to Van Orman et al., 2014; Cherniak, 2010). This mixture was first heated in a Pt crucible at 970 °C for 48 hr and reground before use in the diffusion experiment. A single polished crystal slab was then placed in an open Pt capsule and surrounded by Mg source powder (Fig. 1). The Pt capsule dimensions were $\sim$ 6 mm in length with an outer diameter of 4.5 mm with a triple-crimped and welded bottom. After loading the crystal and source powder, the Pt capsule was crimped shut.

For the duration of the experiment, the experimental assembly was placed in the hotspot of a Deltech 1-atm gas mixing vertical furnace at Arizona State University's Experimental Petrology and Igneous Processes Center (EPIC) lab at constant temperature. Experiments were conducted in air with no oxygen or hydrogen fugacity buffering at temperatures between 800–1150 °C (spaced every 50 °C) for 1 hr to 8 wk with the lower temperature experiments requiring the longer durations. In order to test if the analytical technique used added significant bias to the measured diffusivity, a "zero-time" experiment was run at 950 °C (after Cherniak, 1996). The zero-time experiment was prepared as all the other diffusion experiments, brought to temperature, and then immediately quenched. In all experiments, temperature was monitored using a B-type thermocouple (Pt6Rh vs Pt30Rh) with temperature uncertainties of $\pm$ 1–2 °C. Experimentally annealed crystals were removed from the furnace, quenched in air, and then removed from the crucible and rinsed in an ultrasonic bath of ethanol and water. Crystals were then mounted in indium and gold-coated with polished face up for depth profiling by secondary ion mass spectrometry (SIMS).

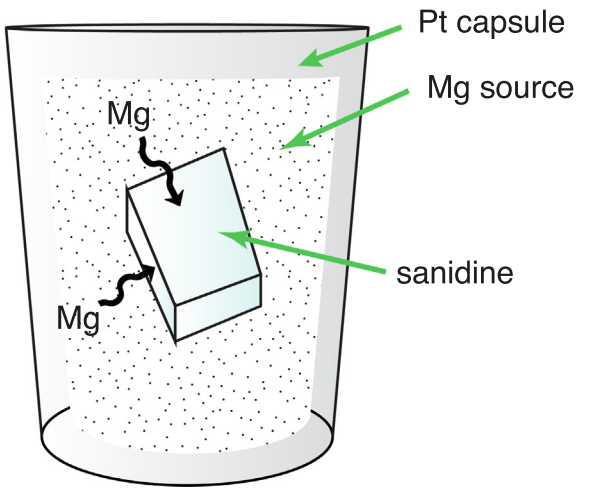

Fig. 1. Schematic of the experimental assembly for diffusion experiments. Natural polished sanidine was surrounded by Mg source powder in a Pt capsule. Experimental assembly was heated to magmatic temperatures to promote Mg to diffuse into the crystal.

2.2. Electron microprobe analysis of sanidine compositions

The composition of the sanidine prior to the experiments were determined via wavelength-dispersive spectrometry using the JXA-8530F Electron Probe Micro-Analyzer (EPMA) at the Eyring Materials Center at Arizona State University. The EPMA was operated at 15 kV and 15 nA using a 10 μm beam diameter to measure major elements (including Ba) in the two sanidine compositions used for experiments (Table 1). Transects were performed across representative samples of crystal slabs to check for chemical homogeneity prior to experiments. The reproducibility of standards was typically better than 1% relative for concentrations > 10 wt% and 10% relative for concentrations of 0.1–1 wt%, thus error is conservatively reported as $\pm$ 0.1 wt% for BaO concentration, and 1 mol% for orthoclase content.

2.3. SIMS depth profiling analysis to obtain diffusion profiles

Depth profiles of major elements such as Na, K, and Si in addition to Mg were performed using the Cameca IMS 6f Secondary Ion Mass Spectrometer (SIMS) in the NSF National SIMS-NanoSIMS Facility at Arizona State University. An O_2^- primary ion beam was generated in a duoplasmatron and accelerated to −12.5 keV. The sample was held at +5000 V thus giving a total impact energy of 8750 eV per nucleon on the sample surface. The primary beam was set at a current near 20 nA, focused to a spot, and rastered over an area 125 × 125 μm^2, leaving a sputtered crater with a flat surface and steep walls. A 400 μm field aperture was used to limit ions allowed into the secondary magnet to a circular area in the middle of the crater 15 μm in diameter to ensure that ions from the crater walls (reflecting all depths) were not sampled. Mass resolution power was set to 800. Positive secondary ions of ^{24}Mg, ^{23}Na, ^{30}Si, and ^{39}K with 0 ± 20 eV excess kinetic energy were detected (no energy filtering applied). When other elements listed below were added to the analysis recipe, we selected ions with 75 ± 20 eV initial kinetic energy (conventional energy filtering, used to remove molecular ions from the mass spectrum). A second measurement of $^{30}Si^+$ was included in analyses examining ions with 75 ± 20 eV for the purpose of normalizing trace species to a matrix ion. Peaks for the different isotopes were detected by either the electron multiplier (EM) or Faraday Cup (FC) secondary ion detectors in the following order: ^{23}Na (1 s, FC/EM), ^{24}Mg (2 s, EM), ^{30}Si (1 s, EM), ^{39}K (1 s, FC), and in some cases, ^{40}Ca (1 s, EM), ^{88}Sr (1 s, EM), ^{138}Ba (1 s, EM). NIST glasses (610, 612, 614) were used to calibrate the Mg, Sr, and Ba concentrations in sanidine. In order to compensate for sample charging throughout the analyses, the magnetic field was moved to detect ^{30}Si and

the sample voltage was ramped from 5080 to 4980 V every 5th cycle. The sample voltage was placed at the centroid of the voltage vs secondary ion intensity curve. To check the effects of ion mixing, depth profiles were obtained from both a zero-time experiment and a raw crystal (unannealed and not exposed to the furnace or any source powder). Additionally, a sanidine that was annealed but not exposed to source powder was analyzed to determine the inherent Mg concentration in Eifel sanidine. In a couple of cases, depth profiles were measured in the same diffusion experiment to check for reproducibility of diffusion coefficients. A single cycle took ~ 20 s, including waiting time to settle the magnetic field at each mass. Each cycle of measurement counted Mg for 2 s. The integrated counts for Mg in each cycle varied from 10,000 (1% precision) to 200 (7% precision).

Following SIMS depth profiling, the depths of the sputtered pits were measured using both a stylus profilometer, as well as the ZeScope optical profilometer in the Eyring Materials Center at Arizona State University. Both profilometers produced precision of 0.7 % and the variation in depth within the central area of the sputtered crater was within 8–40 nm for each pit.

3. RESULTS

3.1. Observations from experimental diffusion profiles

Following our experimental design, the expected solution to the diffusion equation would correspond to the solution to Fick's Second Law involving one-dimensional diffusion in a semi-infinite medium with constant surface concentration (Crank, 1975):

$$\frac{C(x,t) - C_{surf}}{C_{init} - C_{surf}} = erf\,\frac{x}{2\sqrt{Dt}} \quad (1)$$

where C represents the concentration of Mg at depth x after time t, C_{surf} is the constant concentration at the crystal surface, C_{init} is the initial or background concentration inherent to the crystal, and D is the diffusion coefficient. An example fit using this solution to the diffusion equation to our experimental data is shown by the red curve in Fig. 2a. However, Mg concentration gradients in the sanidine experiments display a complex shape rather than a single error function curve (Fig. 2a), where a single fit fails to describe the near-surface portion of the depth profile. Additionally, plotting concentration gradients as inverse error functions (i.e., erf^{-1} [(C(x,t)-C_{surf})/(C_{init}-C_{surf})]) with depth (Fig. 2b) should result in a single linear array if diffusion is constant (Crank, 1975). However, our inverted concentration profiles consistently demonstrate areas where they deviate from linearity (see Supplementary Data S1), which suggests one of two things: 1) artifacts of the analysis technique and/or contamination, or 2) multiple modes of diffusion. For example, the non-linear, near-surface portion of the concentration profile might be unrelated to diffusion and instead an artifact of SIMS reflecting where the composition of the crater floor is reaching a steady-state concentration (with respect to major elements) after the addition of the oxygen primary species and removal/mixing of the gold-coat on the surface into the bulk sample (i.e., SIMS transient zone). Additionally, in many cases a small amount of Mg-rich source material remained adhered to the crystal surface following experimental anneal, regardless of the care taken to analyze clean surfaces, a phenomenon observed in SIMS measurements of other diffusion experiments (e.g., Van Orman et al., 2001, 2014). Measurements related to surface contamination and measurements within

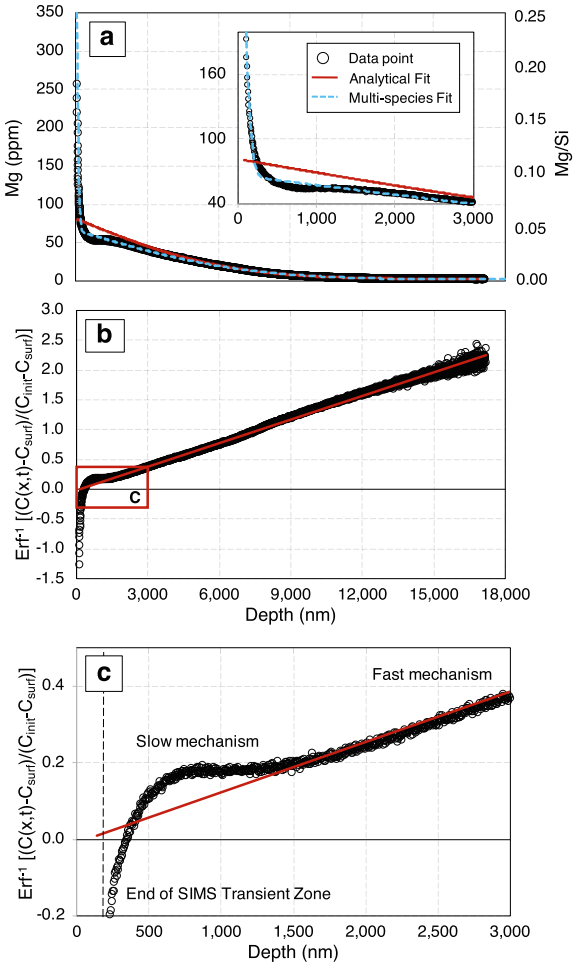

Fig. 2. (a) Mg concentration gradient obtained by SIMS depth profiling on an experimentally-annealed sanidine (Exp. SWAF 237*) displaying a shape that is more complex than an error function curve. The red line represents an example fit using the analytical solution to the diffusion equation, which fails to describe the entirety of the depth profile. The inset is the same plot emphasizing the near-surface portion of the profile. Note the first ~ 100 nm of the profile is not used in the fit because these data are within the SIMS transient zone (see Section 3.1 for more explanation). (b) The same Mg concentration gradient plotted as an inverse error function showing a kink in slope interpreted as the transition between diffusion mechanisms. The red line represents a linear regression that does not fit the near-surface portion of the profile, similar to observed in Fig. 2a. (c) The first 3000 nm of the inverse error function profile showing greater detail of the change in slope and curvature of inverted data. The vertical dashed black line marks the end of the SIMS transient zone and data before this line are excluded from calculating diffusivity.

the SIMS transient zone are located by comparing the stable (i.e., constant) portion of the Si signal with each depth profile measured on SIMS. These factors prohibit the use of measurement cycles near the crystal surface (on average the first ~ 40 nm of the depth profile and in a couple cases up to the first 200 nm) when calculating diffusivities.

Alternatively, in the cases where the near-surface portion of the depth profile is not within the SIMS transient zone or a result from surface contamination, the second possibility is that non-linear portions of a profile may indicate an inconstant diffusion coefficient potentially as result of multiple modes of diffusion operating simultaneously (e.g., Fig. 2c). Note that the very tail end of a given profile (e.g., at ≥ 15,000 nm in Fig. 2c) likely results from reaching the end of the Mg chemical gradient, as well as low Mg count rates. Plotting all of the collected depth profiles as inverse error functions (Supplementary Data S1) consistently display curvature and/or at least an order of magnitude change in slope at depths between 50–500 nm (average 100 nm) while excluding data from the SIMS transient zone (e.g., Fig. 2b, 2c). These depths generally correspond to an abundance > 10 ppm Mg (average 140 Mg ppm) regardless of the experimental temperature and duration. Therefore, data are treated as representing two modes of diffusion (slow and fast) operating simultaneously with the slow diffusion regime dominantly represented in the near-surface of the crystal (Fig. 2c).

Fig. 2 demonstrates how fitting a single analytical solution to the measured depth profiles fails to describe the profile as a whole, specifically the near-surface portion. One approach could be to fit the longer portion of the profile (i.e., the inferred fast-path portion) as a single analytical solution, subtract this contribution from the composite profile, then fit the remaining shorter portion (i.e., near-surface or inferred slow-path portion) to a separate analytical solution. The changes in slope observed in the inverted profiles that indicate a change in diffusion mechanism could then act as a guide to identify the boundary between one analytical fit to another. However, while the near-surface portion of the profile may be dominantly reflecting slow-path diffusion, fast-path diffusion should theoretically be operating simultaneously throughout the entire profile. Therefore, it would be an oversimplification to assume that the near-surface portion of the profile is only controlled by slow-path diffusion, and a more thorough modeling approach is indicated.

3.2. Multi-species diffusion modeling

Diffusion in a crystalline solid occurs from an exchange of position between an atom (or ion) and a crystal defect (e.g., vacant or interstitial site). Therefore, two mechanisms for diffusion of an atom can arise either because it exchanges with two different kinds of defects, or because the atom itself occupies two different types of sites (Dohmen et al., 2010). Such diffusion behavior has been observed in other silicate minerals such as olivine (Dohmen et al., 2010) and garnet (Bloch et al., 2015; Bloch et al., 2020). Dohmen et al. (2010) first developed a model considering two diffusion mechanisms by means of exchange reactions for Li in olivine. In the following section we present a model that corresponds to multi-site diffusion reactions (after Dohmen et al., 2010, Jollands et al., 2019, Bloch et al., 2020), and is tailored to Mg exchange reactions likely to occur in the sanidine crystal structure. This model is intended to replace a single analytical solution to the diffusion equation (i.e., Eq. (1)), which fails to describe the full extent of the measured depth profiles with complex shapes.

There is more than one possible exchange reaction by which Mg can be incorporated into the $KAlSi_3O_8$ sanidine structure. This includes

$$BaMg_{int}Al_{vac}Si_3O_8 = BaMgSi_3O_8 \quad (2)$$

where Mg is present on both an interstitial site (Mg_{int}) coupled with an Al site vacancy (Al_{vac}) as shown in the left side of the equation, and Mg is present on the Al site within sanidine shown on the right side of the equation. Similar reactions to Eq. (2) could be written using other divalent cations sitting on the metal site including Sr or Ca (although Eifel sanidine in these experiments are relatively Ca-poor). In Kröger-Vink notation, Eq. (2) can then be written as

$$Mg_{int}^{\cdot\cdot} + V_{Al}^{'''} = Mg_{Al}^{'} \quad (3)$$

where V is an abbreviation for vacancy, the subscripts for each species indicates the site it occupies, and the • and ′ superscripts indicate an associated positive or negative charge relative to the species normally occupying the site. Writing Eq. (2) as Eq. (3) allows for the isolation of the species that are the most mobile in the reaction, therefore cations sitting on the metal site such as K, Na, Ba, etc. are negated. Assuming that the relevant point defects in this exchange reaction obey Henry's Law, the corresponding mass action law can be written as

$$\log(K) = \log\left(\frac{[Mg_{Al}^{'}]}{[Mg_{int}^{\cdot\cdot}] * [V_{Al}^{'''}]}\right) \quad (4)$$

where K is the equilibrium constant that relates the atomic concentrations (i.e., atoms per formula unit or apfu) of the exchanging species indicated by square brackets. Following the approach outlined by Dohmen et al. (2010), a general equation for the diffusion–reaction process described above can be written as

$$\frac{\partial C_j}{\partial t} = \frac{\partial}{\partial x}\left(D_j \frac{\partial C_j}{\partial x}\right) + R_j \quad (5)$$

where C_j is the concentration of species j, D_j is the diffusion coefficient of species j, t is time, x is distance, and $R_j = r$, for $j = \{Mg_{Al}^{'}\}$; $Rj = -r$, for $j = \{Mg_{int}^{\cdot\cdot}, V_{Al}^{'''}\}$; and r is the time dependent net rate of production of Mg on the metal sites by jumps from interstitial sites (Dohmen et al., 2010). This relationship is used to model the profiles such that, when the equilibrium concentrations described by Eq. (4) are approached, the rates R_j tend to zero and this variable becomes negligible.

Diffusion was modeled numerically following a two-step explicit finite difference algorithm for one-dimension diffusion in plane sheet geometry (Crank, 1975). Each diffusant

was assumed to have homogenous initial concentrations prior to the diffusion run, and a fixed surface concentration throughout the experiment. At each time step, diffusion was allowed to occur solely in response to the individual concentration gradient of each diffusant, and then concentrations at each grid point were re-arranged in order to satisfy Eq. (4) assuming instantaneous local equilibrium. Therefore, local mass and site balance are described by

$$TotalV = [Mg'_{Al}]_{old} + [V'''_{Al}]_{old} = [Mg'_{Al}]_{new} + [V'''_{Al}]_{new} \quad (6)$$

$$TotalMg = [Mg'_{Al}]_{old} + [Mg''_{int}]_{old} = [Mg'_{Al}]_{new} + [Mg''_{int}]_{new} \quad (7)$$

where the subscript *old* denotes concentrations obtained after immediately preceding each time step of diffusion, and subscript *new* is the updated concentrations that are determined by simultaneously solving Eqs. (4), (6) and (7). At a given grid point in the numerical model, Total V is the number of vacant positions on the Al crystal site plus those occupied with Mg, and Total Mg is the total number of Mg atoms per formula unit of sanidine. Solutions were obtained by running the numerical model described above within the context of a non-linear, least-squares optimization routine implemented in Matlab (after Bloch et al., 2020). This model produces 10 free parameters (see Supplementary Data S1), including the diffusivities of each species and their surface and background concentrations in addition to the equilibrium constant that satisfies Eq. (4). Although we have interpreted the observed profiles as conforming well to Eq. (3), there are other exchange reactions that could be derived and modeled and potentially produce satisfactory fits to the observed profiles.

It is not entirely clear how to best produce error estimates for this type of model. The numerical code used to determine diffusivity is computationally time-intensive (i.e., takes a few hours per model and up to 10+ hours in the case of the longer depth profiles). Therefore, determining an error estimate from a Monte Carlo simulation (for example) would take months to run. In lieu of this, we apply an approximate universal error of ± 0.2 log units to the calculated diffusion coefficients, as this is the average error estimate from Monte Carlo simulations when using an analytical solution to the diffusion equation relying on the uncertainty in the depth measurement of the sputtered pit as well as the uncertainty on Mg measurements from SIMS.

3.3. Diffusivity of Mg in sanidine

The diffusion coefficients determined from each experiment are presented in Table 2 and shown by the Arrhenius plots in Fig. 3. Diffusivities for each orthoclase composition and each diffusion mechanism (i.e., slow and fast) are fit separately to the Arrhenius equation:

$$log_{10}D = log_{10}D_0 - \frac{E_A}{RT} \quad (8)$$

where D is the determined diffusion coefficient, D_0 is the pre-exponential factor, E_A is the activation energy, R is the gas constant, and T is temperature in K. Arrhenius parameters determined from 25 experiments and 32 depth profiles are summarized in Table 3 and categorized by diffusion mechanism (i.e., fast/slow) and composition.

The Arrhenius parameters determined from fitting the diffusion coefficients for Or_{71} include an activation energy of 275 ± 14 kJ mol^{-1} (2σ) and pre-exponential factor of 4.2×10^{-6} m^2 s^{-1} for fast-path diffusion and 369 ± 15 kJ mol^{-1} (2σ) and pre-exponential factor of 1.4×10^{-5} m^2 s^{-1} for slow-path diffusion. When fitting the diffusion coefficients for Or_{82}, an activation energy of 283 ± 14 kJ mol^{-1} (2σ) and pre-exponential factor of 1.6×10^{-5} m^2 s^{-1} are obtained for fast-path diffusion and an activation energy of 405 ± 15 kJ mol^{-1} (2σ) and pre-exponential factor of 3.9×10^{-4} m^2 s^{-1} are obtained for slow-path diffusion. Of the two crystallographic orientations investigated for both Or_{71} and Or_{82} (*c*-parallel and *c*-perpendicular), the diffusion coefficients are within approximate error of each other suggesting isotropic diffusion of Mg in the compositions of sanidine investigated.

Fast-path diffusion of Mg in sanidine is at least three orders of magnitude faster than slow-path diffusion as determined for both Or_{71} and Or_{82}. In addition, diffusion coefficients determined for fast-path diffusion in Or_{71} are within approximate error of the fast-path diffusion coefficients determined for Or_{82}. The same is true when comparing slow-path diffusion coefficients between Or_{71} and Or_{82}. Additionally, the activation energies for fast-path diffusion of Or_{71} and Or_{82} are indistinguishable of each other when considering approximate error estimates. Activation energies for slow-path diffusion in both sanidine samples are similarly larger than the activation energies for slow-path diffusion, however the Or_{71} and Or_{82} compositions yield distinct values given approximate error estimates. Although the compositional range of sanidine is relatively narrow (i.e., 11 mol%) the results suggest there is little to no resolvable compositional dependence of Mg diffusion on major element chemistry (i.e., relative K-Na content) in sanidine. However, a more comprehensive study encompassing a broader alkali feldspar range is required to confirm this.

3.4. Time dependence of diffusion

In order to determine whether lattice diffusion is the dominant process being measured, we performed a time-series and a zero-time experiment on both compositions of feldspars (after Cherniak, 1996, Cherniak, 2002, Van Orman et al., 2014, Bloch et al., 2015). Fig. 4 shows the results of the time-series study displaying both fast- and slow-path *c*-parallel diffusion. The calculated diffusion coefficients from the time-series (i.e., SWAF 263 and 255) are reported in Table 2 and agree within 2σ approximate error for experimental run durations varying from a few to over 50 days. Fig. 5 compares the depth profiles between a diffusion experiment, zero-time experiment, and a raw crystal (of which did not have contact with a Mg source and was not annealed in a furnace). The zero-time experiments show little to no uptake of Mg in short anneals relative to profiles measured in diffusion experiments and raw crystals. This behavior is observed in both Or_{71} and Or_{82}, confirming that measured concentration profiles are the result of diffusion only.

Table 2
Experimental conditions and results.

Exp. ID	T (°C)	Time (s)	Orientation°	Composition	$Log_{10}D_1$ (m^2 s^{-1})	$Log_{10}D_2$ (m^2 s^{-1})	2σ
SWAF 260c	1149	1.09×10^4	$c_{\parallel}$	Or_{71}	−15.05	−18.18	0.2
SWAF 268	1099	1.44×10^4	$c_{\parallel}$	Or_{71}	−15.45	−19.10	0.2
SWAF 261c	1049	3.60×10^4	$c_{\parallel}$	Or_{71}	−16.67	−19.32	0.2
SWAF 257c	1002	8.64×10^4	$c_{\parallel}$	Or_{71}	−16.98	−19.54	0.2
SWAF 258c	953	8.64×10^4	$c_{\parallel}$	Or_{71}	−17.40	−20.91	0.2
SWAF 263 1	853	2.42×10^6	$c_{\parallel}$	Or_{71}	−17.86	−21.70	0.2
SWAF 263 2	853	1.21×10^6	$c_{\parallel}$	Or_{71}	−18.10	−21.65	0.2
SWAF 263 3	853	6.05×10^5	$c_{\parallel}$	Or_{71}	−18.06	−21.89	0.2
SWAF 271 71	805	4.56×10^6	$c_{\parallel}$	Or_{71}	−18.38	–22.98	0.2
SWAF 271 71 *	805	4.56×10^6	$c_{\parallel}$	Or_{71}	−18.87	–22.62	0.2
SWAF 259b	1100	1.44×10^4	$c_{\perp}$	Or_{71}	−15.72	−19.18	0.2
SWAF 261b	1049	1.44×10^4	$c_{\perp}$	Or_{71}	−16.44	−19.23	0.2
SWAF 257b *	1002	3.60×10^4	$c_{\perp}$	Or_{71}	−16.80	−19.99	0.2
SWAF 264 71	902	8.64×10^4	$c_{\perp}$	Or_{71}	−17.82	−21.69	0.2
SWAF 264 71 *	902	5.97×10^5	$c_{\perp}$	Or_{71}	−17.53	−21.31	0.2
SWAF 233	1150	1.19×10^4	$c_{\parallel}$	Or_{82}	−15.02	−18.21	0.2
SWAF 186	1105	1.66×10^4	$c_{\parallel}$	Or_{82}	−15.15	−18.25	0.2
SWAF 203	1052	3.55×10^4	$c_{\parallel}$	Or_{82}	−16.36	−19.36	0.2
SWAF 159	1001	8.68×10^4	$c_{\parallel}$	Or_{82}	−16.15	−20.00	0.2
SWAF 159 †	1001	8.68×10^4	$c_{\parallel}$	Or_{82}	−16.45	−20.45	0.2
SWAF 136	946	8.57×10^4	$c_{\parallel}$	Or_{82}	−17.39	−20.76	0.2
SWAF 136 †	946	8.57×10^4	$c_{\parallel}$	Or_{82}	−17.51	−21.00	0.2
SWAF 264 82	902	5.97×10^5	$c_{\parallel}$	Or_{82}	−17.30	−21.82	0.2
SWAF 264 82 †*	902	5.97×10^5	$c_{\parallel}$	Or_{82}	−17.51	−21.82	0.2
SWAF 255 1	850	2.41×10^6	$c_{\parallel}$	Or_{82}	−17.77	–22.34	0.2
SWAF 255 2	850	1.21×10^6	$c_{\parallel}$	Or_{82}	−17.41	−21.89	0.2
SWAF 255 3	850	4.27×10^5	$c_{\parallel}$	Or_{82}	−17.69	–22.00	0.2
SWAF 271 82	805	4.56×10^6	$c_{\parallel}$	Or_{82}	−18.79	–22.58	0.2
SWAF 240	1051	8.66×10^4	$c_{\perp}$	Or_{82}	−16.19	−19.57	0.2
SWAF 237	1002	8.68×10^4	$c_{\perp}$	Or_{82}	−16.52	−19.69	0.2
SWAF 237 *	1002	8.68×10^4	$c_{\perp}$	Or_{82}	−15.74	−19.45	0.2
SWAF 239	950	8.68×10^4	$c_{\perp}$	Or_{82}	−17.12	−21.20	0.2

° Indicates orientation in which diffusion was measured.
† Duplicate analysis for reproducibility.
* Deeper depth profiles measured for longer duration.

4. DISCUSSION

4.1. Comparison to Mg diffusion in plagioclase and other cation diffusion in feldspar

An important outcome of this study is the ability to compare Mg diffusion in sanidine with plagioclase. A summary of experimentally-determined diffusivities for Mg in feldspar is shown in Fig. 6. Previous work finds that Mg diffusion in plagioclase (An_{23}–An_{93}) is dependent on major element chemistry, where diffusivity increases with increasing albite content (i.e., relative Na; Van Orman et al., 2014). Similarly, for the case of Sr diffusion in sanidine, significant differences in Arrhenius parameters have been found when comparing sanidine with large differences in K-Na contents suggesting some compositional dependence on diffusion (Fig. 7; Cherniak and Watson, 1992). Mg diffusion in sanidine determined in this study reveal diffusion coefficients within approximate error of each other for two different sanidine compositions (Or_{71} and Or_{82}), suggesting there is little to no resolvable major element dependence in sanidine, unlike Sr diffusion in sanidine and Mg diffusion in plagioclase. However, because the compositional range examined in this study is relatively small (11 mol% Or) further investigations over a broader range of sanidine compositions would be required to confirm this observed behavior. Mg diffusion in plagioclase displays weak anisotropy between the *b* and *c* directions observed in labradorite and anorthite, however it is generally advised to treat Mg diffusion in plagioclase as isotropic (LaTourrette and Wasserburg, 1998; Van Orman et al., 2014). Of the two crystallographic orientations investigated for Mg diffusion in sanidine in this study (*c*-parallel and *c*-perpendicular), there is no resolvable difference in diffusivities or diffusion parameters suggesting Mg diffuses isotropically in sanidine for the orientations and compositions investigated. These data thus far suggest feldspar crystallographic orientations do not play a significant role in controlling Mg diffusion in feldspar.

Another similarity between Mg diffusion in sanidine and plagioclase are the Arrhenius parameters shared between fast-path sanidine diffusion and plagioclase diffusion. Not only are the absolute fast-path diffusivities similar to those in plagioclase (Fig. 6), but the activation energies for fast-

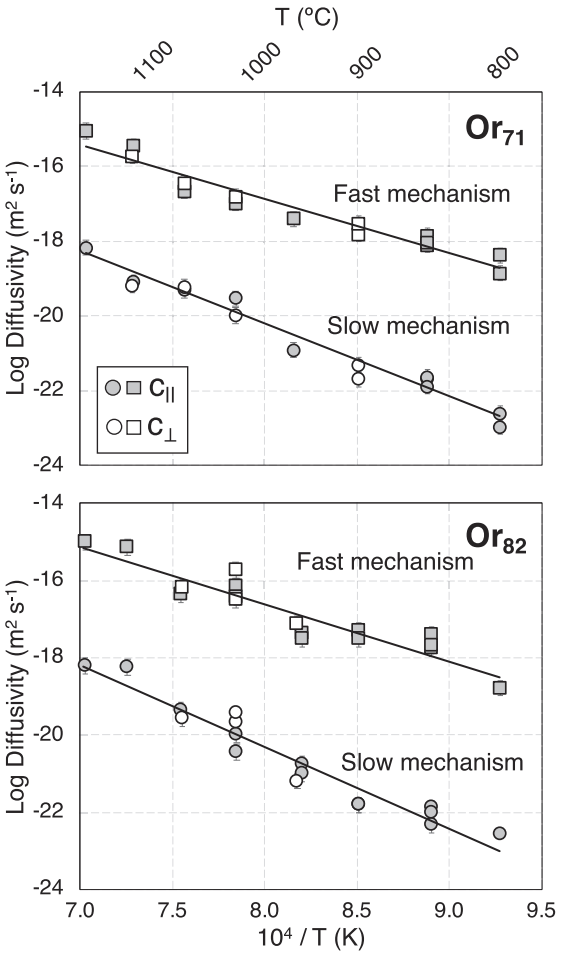

Fig. 3. Arrhenius plot for Mg diffusion in Eifel sanidine Or_{71} (top panel) and Or_{82} (bottom panel) showing the two crystallographic orientations investigated (diffusion measured both parallel and perpendicular to *c* axis). Linear regressions for each dataset are shown by solid black line and the associated Arrhenius parameters are reported in Table 3.

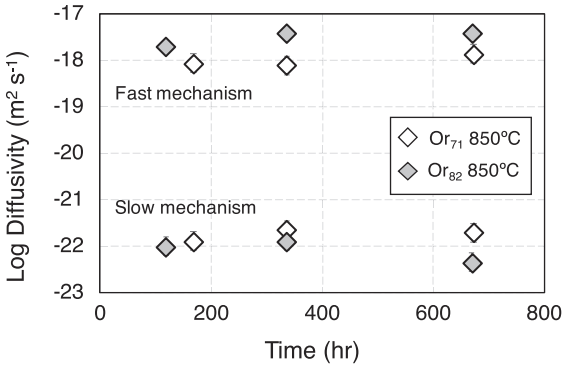

Fig. 4. Effect of anneal time on calculated Mg diffusion rates (Exps. SWAF 263 and 255) in Eifel sanidine (Or_{71} and Or_{82}) from Table 2. The diffusion coefficients determined from experiments with different anneal times are the same within approximate error (2σ).

path diffusion in sanidine of 275 ± 14 (Or_{71}) and 283 ± 14 kJ mol^{-1} (Or_{82}) are indistinguishable from Mg diffusion in plagioclase ($An_{23\text{-}93}$) of 287 ± 10 kJ mol^{-1} at relevant temperatures (Fig. 6 Van Orman et al., 2014). Additionally, Mg diffusion in An_{95} investigated at relatively higher temperatures and at two crystallographic orientations have activation energies of 254 and 278 ± 43 kJ mol^{-1} (LaTourrette and Wasserburg, 1998), both of which are within approximate error of the activation energies in this study. An additional study of Mg diffusion in plagioclase (An_{60}) investigated at relatively higher temperatures yields a slightly higher activation energy of 320 kJ mol^{-1} with no reported error that is close but not within approximate error of Mg in sanidine (Faak et al., 2013). For the most part, the present data suggests fast-path Mg diffusion in sanidine behaves similarly if not the same to Mg diffusion in plagioclase.

An important and unique outcome of this study is the discovery of a slow-path diffusion mechanism in sanidine that differs greatly from that of fast-path Mg diffusion in sanidine and Mg diffusion in plagioclase (Fig. 6). Irregularly shaped Mg concentration gradients observed in sanidine suggest multi-mode diffusion mechanisms operating simultaneously (fast and slow), which is a phenomenon not previously observed for Mg diffusion in plagioclase experiments. One possibility is that the measurements from Van Orman et al. (2014) were unable to observe slow-path diffusion (if present in plagioclase) because of anneal times that were on average 3 days (relative to an average of 9 days in this study) and no more than 3 weeks (relative to 8 weeks in this study) for their lower temperature experiments. However, diffusion distances generally scale as the square root of time, and diffusion distances in the shorter experimental durations of Van Orman et al. (2014) would be about 60% of the diffusion distance for the longer times and therefore slow-path Mg diffusion should still be detectable if present. Van Orman et al. (2014) do not explicitly report irregular depth profile shapes but do make note of near-surface irregularity when inverting their depth profiles, which is attributed to surface contamination. While surface contamination is a challenge posed by diffusion

Table 3
Calculated diffusion parameters.

Composition	Mechanism	log D_0 (m^2 s^{-1})	2σ	E_A (kJ mol^{-1})	2σ	R^2
Eifel Or_{71}	*fast*	4.2E-06	5.6E-06	275	14	0.94
	slow	1.4E-05	1.9E-05	369	14	0.97
Eifel Or_{82}	*fast*	1.6E-05	2.4E-05	283	15	0.94
	slow	3.9E-04	5.8E-04	405	15	0.94

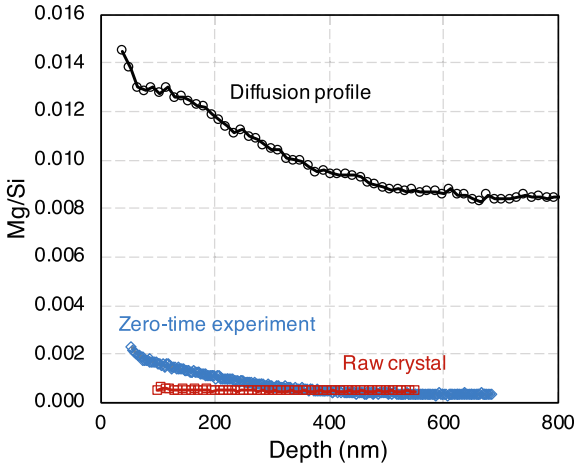

Fig. 5. Compilation of depth profiles measured from raw Eifel sanidine (has not been in contact with a Mg source, nor been annealed in a furnace), a zero-time experiment (brought to temperature surrounded by powder then rapidly quenched), and a diffusion experiment. Zero-time experiments show little to no uptake of Mg relative to a raw crystal and a diffusion experiment, confirming that concentration profiles are related only to diffusion. Note that profiles start at different depths as a result of discarding initial analyses affected by surface contamination and/or SIMS artifacts, the extent of which varies between analyses, see Section 3.1 for further explanation.

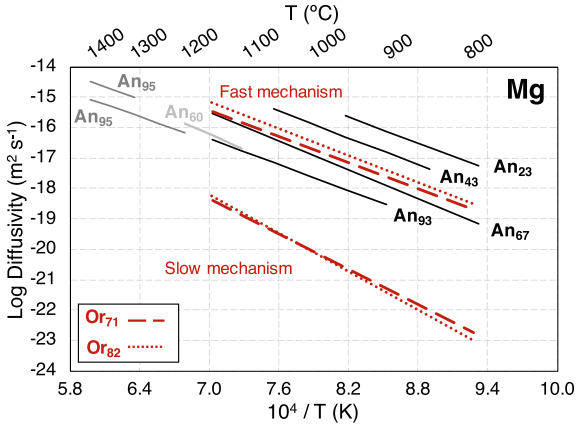

Fig. 6. Summary of Mg diffusion in feldspar. Data from this study are shown by red dashed and dotted lines showing both fast- and slow-path diffusion. Data for Mg diffusion in plagioclase are shown by solid black and grey lines ($An_{23,\ 43,\ 67,\ 93}$; Van Orman et al., 2014, An_{60}; Faak et al., 2013, An_{95} diffusion normal to (010) and (001); LaTourrette and Wasserburg, 1998).

experiments, it is possible that the analytical model applied to those depth profiles are potentially missing a present slow-path diffusion mechanism by ignoring near-surface information. This of course would require further investigation and the application of a multi-site diffusion reaction model as employed in this study.

Fig. 7 shows a summary of experimentally-determined cation diffusivities for feldspar at relevant temperatures to this study. The slow-path diffusivities of Mg in sanidine plot

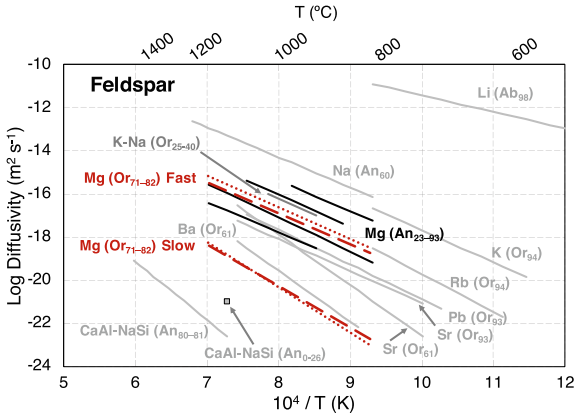

Fig. 7. Summary of cation diffusion in feldspar with relevant compositions to those investigated in this study. Mg diffusion in sanidine determined in this study is shown by red dashed and dotted lines. Mg diffusion in plagioclase are shown by black solid lines (Van Orman et al., 2014). Other cation diffusion in feldspar are shown by solid gray lines (Li in Ab_{98}; Giletti and Shanahan, 1997, Na in An_{60}; Behrens et al., 1990, Na-K interdiffusion in $Or_{25\text{-}40}$; Christoffersen et al., 1983, K in Or_{94}; Foland, 1974, Rb in Or_{94}; Giletti, 1991, Pb in Or_{93}; Cherniak, 1995, Sr in Or_{61} and Or_{93}; Cherniak and Watson, 1992, Ba in Or_{61}; Cherniak, 2002, CaAl–NaSi interdiffusion in An_{80}; Grove et al., 1984, CaAl-NaSi interdiffusion in $An_{0\text{-}26}$ at dry conditions; Yund, 1986).

near Ba diffusion in sanidine (Or_{61}). When comparing activation energies, slow-path Mg diffusion for both Or_{71} and Or_{82} (369 ± 14 and 405 ± 15 kJ mol^{-1}) have lower activation energies than Ba (455 ± 20 kJ mol^{-1}). When considering atomic radii, it is excepted that the smaller Mg ion (0.89 Å VIII-fold) would diffuse faster than the larger Ba ion (1.42 Å VIII-fold; Shannon, 1976), which is a common observation when comparing different element-mineral pairs (Fig. 7). This predicted behavior is true for fast-path Mg diffusion in sanidine, however slow-path Mg diffusion has comparable Arrhenius parameters to that of the relatively larger Ba and Sr, in addition to having slower absolute diffusivities than Ba. Cation charge is also an important factor to consider in conjunction with atomic radii. For example, while K and Ba have similar ionic radii (1.51 and 1.42 Å VIII-fold), K^+ diffuses faster than Ba^{2+}. Slow-path Mg^{2+} diffusion appears to follow this same pattern, diffusing slower than monovalent Na, K, and Li in sanidine and at similar rates to divalent Ba but slightly slower than divalent Sr. Fast-path Mg^{2+} diffusion in sanidine is comparable to monovalent Rb diffusion in sanidine and also displays similar activation energies (Rb $E_A = 340 \pm 33$ kJ mol^{-1}; Fig. 7). In the next section, we will explore mechanisms that are potentially responsible for the observed fast- and slow-path diffusion of Mg in sanidine.

4.2. Multi-mode diffusion mechanisms

The model produced in this study assumes that Mg can migrate both by interstitial sites (i.e., fast-path diffusion) and by an Al site, of which is a framework site in the sanidine structure (i.e., slow-path diffusion).

Charge-compensating species are necessary to facilitate exchange of divalent cations (i.e., Mg^{2+}) with predominant structural cations such as K, Na, and Al in alkali feldspar. In contrast, Mg in plagioclase can migrate by direct exchange with divalent Ca (Cherniak, 2002; note that Ca was not detectable by electron probe analysis in Eifel sanidine used for experiments; Table 1). Therefore, movement of charge-compensating species may impose a rate-limiting factor on diffusion of divalent species in alkali feldspars. Fast-path Mg diffusion in sanidine is a more anticipated result when comparing to known Mg diffusion in plagioclase, however the cause behind slow-path Mg diffusion in sanidine is undetermined. A possible mechanism for slow-path Mg^{2+} diffusion in the sanidine structure is charge compensation via framework elements, such as Si and Al in tetrahedral sites and K and Na on the M site (e.g., Parsons and Lee, 2005):

$$Mg^{2+} + Al^{3+} = (K^{+}, Na^{+}) + Si^{4+} \quad (9)$$

A similar reaction exists in plagioclase: the interdiffusion of CaAl-NaSi, which is much slower than that of single cation diffusion in plagioclase and has a high activation energy (516 kJ mol^{-1}; Grove et al., 1984). This is unsurprising when considering the energy required to break a Si-O bond (Fig. 7; Grove et al., 1984; Yund, 1986). Slow-path Mg diffusion in sanidine is not nearly as slow as CaAl-NaSi interdiffusion in plagioclase. It should be noted that Eifel sanidine is known to display rapid Al-Si ordering/reordering, which would have potential to enhance diffusion and potentially explain why the slow-path Mg mechanism is faster than CaAl-NaSi interdiffusion in plagioclase (Parsons and Lee, 2005). However, the act of pre-annealing Eifel sanidine prior to experimental diffusion experiments as was done here has been shown to reduce Al-Si reordering and likely mitigates this effect (Bertelmann et al., 1987; Bernotat-Wulf et al., 1988; Parsons and Brown, 1991; Parsons and Lee, 2005). It is difficult to evaluate Al and Si behavior in our diffusion experiments given the high abundance of these framework-forming species compared to the trace amounts of Mg, such that any small changes are undetectable via SIMS or electron probe. Additionally, given the differences in ionic radii between Mg with Na and K, it is unlikely that Mg exchanges for K and/or Na on the sanidine M site.

A more energetically favorable reaction that does not involve the exchange of Si is

$$(Ba, Sr)^{2+} + Mg^{2+} \leftrightarrow (K, Na)^{1+} + Al^{3+} \quad (10)$$

where divalent Ba or Sr (both of which are abundant in Eifel sanidine and natural volcanic sanidine in general; Table 1) exchange for a K on the metal site due to similar ionic radii (Ba = 1.42, Sr = 1.26, K = 1.51 Å VIII-fold coordination), and Mg exchanges with an Al on an Al site given their comparable ionic radii. Although the exact diffusion rate of Al diffusion in feldspars is unknown, the involvement of Al migrating from a tetrahedral site in this reaction likely slows the migration of Mg. The involvement of K and Na does not likely impose a rate-limiting control on Eq. (1) because diffusivities and Arrhenius parameters for K diffusion and K-Na interdiffusion in alkali feldspar are approaching or are similar to fast-path Mg diffusion (~285 kJ mol^{-1}; Fig. 7; Christoffersen et al., 1983, Foland, 1974). However, the involvement of larger cations such as abundant Ba and Sr may place a rate-limiting control on slow-path Mg diffusion (see Fig. 7). In nature, volcanic sanidine commonly contains a relatively high abundance of Ba (thousand to tens of thousands ppm) and Sr (tens to hundreds ppm) (e.g., Hervig and Dunbar, 1992, Zellmer et al., 1999, Anderson et al., 2000, Ginibre et al., 2004, Morgan et al., 2006, Zellmer and Clavero, 2006, Hildreth and Wilson 2007, Stelten et al., 2013, Chamberlain et al., 2014, Bachmann et al., 2014, Till et al., 2015, van Zalinge et al., 2017, Shamloo and Till, 2019, Szymanowski et al., 2019, Landi et al., 2019). Results from this study show Ba diffusivities broadly overlap with slow-path Mg diffusion in sanidine and also have similar Arrhenius parameters to Ba and Sr in sanidine (455 and 450 kJ mol^{-1}; Fig. 7). While it is unfavorable for Mg^{2+} to directly exchange for the more abundant Sr^{2+} and/or Ba^{2+} given the differences in ionic radii, Ba and Sr may still impose a rate-limiting factor on slow-path Mg diffusion as demonstrated by Eq. (10). Ba and Sr both have higher activation energies than slow-path Mg, potentially making slow-path Mg diffusion more sluggish when in the presence of abundant Ba and Sr (Cherniak, 1996; Cherniak, 2002) but is still faster than CaAl-NaSi diffusion because it does not involve Si migration.

To further test this hypothesis, we measured Ba and Sr along with Mg in the depth profiles via SIMS (e.g., Fig. 8). There appears to be a broad negative correlation between Ba and Mg concentration gradients in the near-surface portion of the profile where slow-path diffusion likely dominates the concentration signal relative to the deep portion of the profile (Fig. 8). This observation is true for all the depth profiles that included the measurement of Ba. The relationship between Sr is less straight forward. The example depth profile in Fig. 8 shows the first 400 nm of the Sr signal mimicking Mg behavior, while ~ 400–1200 nm shows a stronger negative correlation to Mg than Ba displayed. The natural sanidine used for experiments are annealed and checked for chemical homogeneity via the electron probe and SIMS prior to the diffusion experiment. Therefore, any chemical gradient that exists in Mg, Sr, and Ba are created only after the diffusion experiment occurs. This potentially suggests that Ba and Sr participate during the diffusion experiment and are in fact migrating with Mg and Al. Statistically it may be argued that the direct interaction between the diffusant and Sr and Ba relative to the probability of encountering the predominant K and Na in sanidine is low. However, based on ionic radii, it is less favorable for Mg to directly exchange with K and Na rather than Al. At present, we conclude that the exchange reaction of Mg for Al coupled with Ba and Sr for K and Na may impose a rate-limiting control on slow-path Mg diffusion. However, the current evidence is not definitive as to the importance and likelihood of Ba- and Sr-limiting slow-path Mg diffusion in sanidine and it requires further scrutiny and experimentation on Ba- and Sr-poor sanidine. Additionally, it may be possible that Ba and Sr also have a second mode of diffusion that is

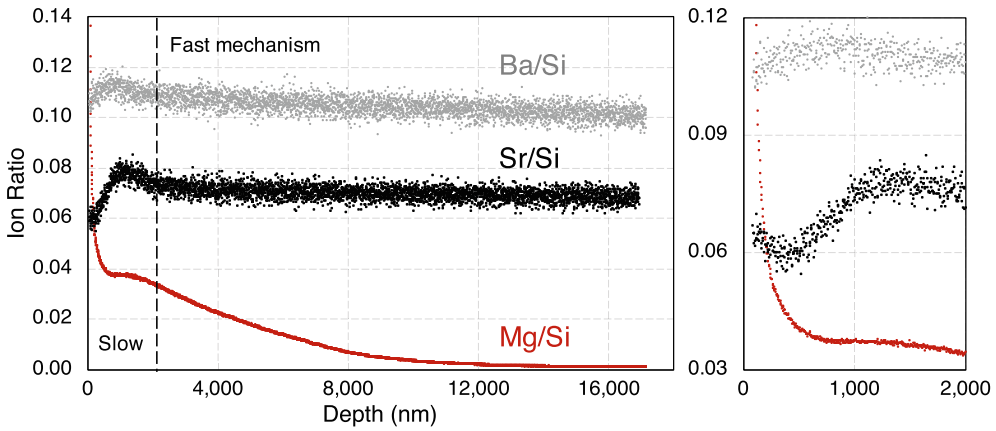

Fig. 8. SIMS depth profiles of Ba, Sr, and Mg measured from a diffusion experiment (Exp. SWAF 237*). Dashed vertical line represents the rough boundary where slow- and fast-path diffusion are likely contributing the most to the SIMS signal. A zoomed in version of the near-surface portion of the profile is shown on the right. Near the crystal surface Mg is broadly negatively correlated with Ba and Sr (with the exception of slight downward diffusion of Sr in the first 300 nm of the profile). The remainder of the profile where fast path diffusion likely dominates appears to be uncoupled with Ba and Sr distribution. Note that data at depths < 100 nm are not included due to SIMS artifacts and/or surface contamination. See Section 3.1 for further explanation.

not recorded in the literature at present. Ba and Sr have similar ionic radii to K making direct substitution on the metal site relatively straight forward. However, these divalent cations may exhibit multi-mode diffusive behavior similar to Mg and include the involvement of multi-site exchange reactions. However, such behavior requires further experimentation.

Lastly, we discuss possible mechanisms responsible for fast-path Mg diffusion in sanidine. Fig. 8 shows that Ba and Sr remain largely constant in the remainder of the profile farthest from the crystal surface, potentially suggesting the fast-path diffusion mechanism is uncoupled to potentially rate-limiting Ba and Sr (and Al). Instead, it is likely that Mg migrates quickly by means of interstitial sites coupled with vacant sites (e.g., Al vacancies) similar to what is implied for Mg diffusion in plagioclase. Longhi and Hays (1979) originally suggested that plagioclase can incorporate excess Si^{4+} in tetrahedral sites, which leads to the formation of large-site vacancies to maintain charge balance. This may have the effect of increasing Mg diffusion rates in plagioclase. The amount of $(K,Na)AlSi_3O_8$, $CaAl_2Si_2O_8$, and Si_4O_8 is likely not changed significantly by diffusion during our experiments as documented by Grove et al. (1984) and if it was it would not be detectable with the analytical tools used in this study. Because the experiments in this study were not buffered for silica activity, we cannot determine if excess silica is a controlling factor in fast-path diffusion of Mg in sanidine as it is for Mg diffusion in plagioclase and provides a goal for future studies.

4.3. Geospeedometry in a natural system: the Lava Creek supereruption, yellowstone

It is worthwhile to examine whether a given experimental setup is an accurate representation of nature. By design, our experiments set up a chemical potential gradient between the MgO source powder and the natural sanidine, where the chemical potential of the powder is much greater than that of the sanidine. For comparison, we examine the relationship between Mg in sanidine rims and the co-existing melt from a fairly typical rhyolite tuff, the ca. 631 Lava Creek Tuff (LCT) at Yellowstone Caldera (Matthews et al., 2015). Glass compositions measured from LCT member B pumice suggest Mg concentrations of ~ 200 ppm (sample 8YC-411, Christiansen, 2001). Measured partition coefficients for Mg between alkali feldspar and rhyolite ($K_D = 0.2–0.8$; Icenhower and London, 1996) suggest that a minimum of ~ 40–160 ppm Mg should be found in a sanidine rim in equilibrium with LCT-B melt. Measured Mg concentration in LCT-B sanidine rims via Nanoscale Secondary Ion Mass Spectrometry (NanoSIMS; see Shamloo and Till, 2019 for analytical details) reveal lower concentrations of ~ 1–2 ppm Mg (e.g., Fig. 9). The chemical potential gradient between LCT-B melt and sanidine rims would therefore promote diffusion from the Mg-rich source (i.e., melt) into Mg-poor sanidine during and after crystallization. Therefore, the conditions set up in our experiments are approximate to those of the LCT-B magma to the best of our ability, although additional considerations such as oxygen and hydrogen fugacity as well as elemental activities would need to be accounted for.

While our experimental design attempts to be representative of a natural system in the case of the LCT, the question remains which Mg diffusion coefficient (i.e., fast-path vs. slow-path) is appropriate for performing geospeedometry to calculate magmatic timescales. The sanidine shown in Fig. 9 has a Mg concentration profile of 1.4 ± 0.2 ppm in the interior that increases to 2.4 ppm Mg in the rim. In order to apply geospeedometry, it must first be determined if the Mg signal measured in the LCT sanidine is dominantly a result from fast- or slow-path diffusion. One approach to assess this is by comparing the concentration gradients of Mg with other known diffusers in sanidine such as Ba and Sr. The sanidine in Fig. 9 shows concentration profiles measured for Ba, Sr, and Mg in the same grain using NanoSIMS. The Mg concentration profile mimics

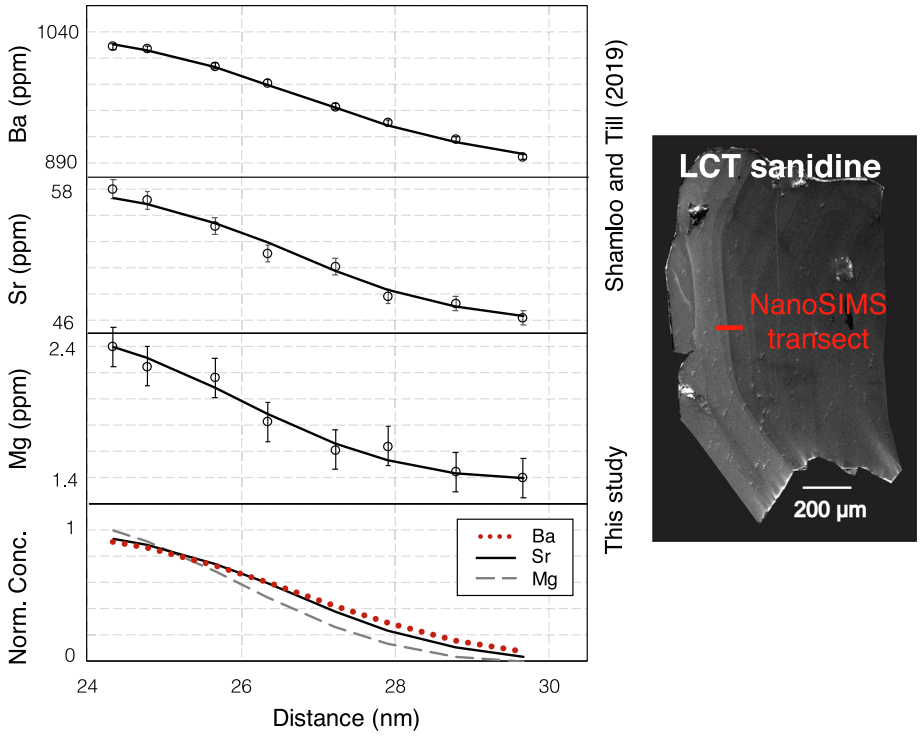

Fig. 9. Elemental concentration gradients measured via NanoSIMS across rim to core (left to right) in zoned sanidine (shown by cathodoluminescence image on the right) from the Lava Creek Tuff (member B) at Yellowstone Caldera. Elemental data are shown as black circles with 2σ error bars and the black curve represents a model fit to data using the analytical solution to the diffusion equation at a specified temperature. Data and models for Ba and Sr are from Shamloo and Till (2019) and Mg data are from this study. The bottom panel shows all three elemental concentration profiles normalized for the sake of comparison.

the shape of Ba and Sr. At the recorded rim temperature (i.e., 814 °C determined from feldspar-liquid thermometry; see Shamloo and Till, 2019 for details), fast-path Mg diffuses at $\sim 10^{-19}$ m^2 s^{-1}, slow-path Mg at $\sim 3 \times 10^{-23}$ m^2 s^{-1}, Sr at 10^{-21} m^2 s^{-1}, and Ba at 4×10^{-23} m^2 s^{-1} (Cherniak and Watson, 1992; Cherniak, 2002). It follows that fast-path Mg > Sr > Ba > slow-path Mg. If the Mg signal in the NanoSIMS profile was a result of predominantly fast-path diffusion it would be expected to be more relaxed in shape compared to Ba and Sr because of its faster diffusivity. In this case, Mg concentrations would approach the detection limit of the NanoSIMS (i.e., 0.6 ppm Mg) within a few seconds at 814 °C, as significant diffusion would cause Mg to migrate across the intracrystalline boundary, making it difficult to identify a distinct profile. Alternatively, if slow-path diffusion was dominantly contributing to the Mg signal, it would be expected to be the same shape and width as the Ba profile because of their similar diffusivities, of which is observed, in addition to having a similar shape to Sr (Fig. 9). Overall, it is difficult to know in which proportion fast- versus slow-path diffusion contributes to the Mg signal given that they operate simultaneously. However, we conclude the Mg signal is likely dominated by slow-path Mg diffusion given the observed behavior when compared to Ba and Sr, as well as the fact that a Mg signal dominated by fast-path Mg diffusion may not be identifiable at such low Mg abundance (a couple ppm) even given the ultra-high-resolution of the NanoSIMS.

Shamloo and Till (2019) attributed identical Ba and Sr profile widths (without the Mg profile) as the result of crystal growth in an evolving magma composition rather than pure diffusion based on known Ba and Sr diffusion behavior. The Mg profile measured here shows that for the case of the LCT-B, significant diffusion is not recorded. This suggests insufficient time has elapsed in order to yield Ba, Sr, and Mg profiles that significantly differ in shape at the level of NanoSIMS resolution. This prohibits the use of traditional diffusion chronometry where it is assumed that an observed concentration profile relaxed from a step-function, but hints towards potentially fast timescales between the inferred rejuvenation and eruption that the slow-moving Ba, Sr, and Mg are unable to capture. Instead, we constrain a maximum possible time interval between sanidine rim growth and eruption by calculating the time required for slow-path Mg to diffusively diverge in shape from Ba and Sr at the resolution of the NanoSIMS analyses after Till et al. (2015). Using the Mg slow-path diffusion coefficient for Or_{71} (most similar to $Or_{\sim 50}$ LCT-B sanidine) at 814 °C, we calculate a maximum timescale between rejuvenation and eruption of 38 years. The same calculation done with the fast-path diffusivity for the same temperature yields a timescale of just 5 weeks. It is difficult to report error associated with these timescales due to the nature of our model (see Section 3.2), however this exercise still provides important constraints on the order of magnitude of timescales. Therefore, we refer to these estimates as a few decades and a few weeks.

An advantage to using a diffusion chronometer with multiple rates and modes is the ability to bracket timescales. As stated before, it is difficult to know to which degree fast- versus slow-path diffusion is contributing to the Mg signal measured in the LCT-B sanidine. However, by calculating a timescale for a scenario in which the signal is 100% slow-path and 100% fast-path provides a bracket of time. Slow-path diffusion reveals that the timing between rejuvenation and eruption can be no more than a few decades, while fast-path diffusion provides potential for timescales on the order of weeks. Shamloo and Till (2019) constrained diffusion timescales from Ti in LCT-B quartz (of which is co-saturated with sanidine) on average of 20 years when using Ti-in-quartz Arrhenius parameters from Cherniak and Watson (2007). Applying newly derived Arrhenius parameters from Jollands et al. (2020) yields much longer timescales on the order of thousands of years. However, these new Ti-in-quartz timescales do not support the observation that LCT sanidine and quartz are co-saturated as thermodynamic modeling and experiments on similar compositions predict (Almeev et al., 2012; Bolte et al., 2015), therefore we favor the timescales originally reported by Shamloo and Till (2019) using Cherniak and Watson (2007) Arrhenius values. The favored Ti-in-quartz timescales align well with the maximum timescale predicted by slow-path diffusion. Fast-path determined timescales as short as weeks, however, may be more in alignment with the explosive nature of the LCT supereruption that likely resulted from quick ascent. It should be noted that mineral textures, such as rim overgrowth that truncate resorbed crystal interiors is observed in both sanidine and quartz, which may support rapid growth and therefore quick timescales (Shamloo and Till, 2019). Additionally, the fact that the concentration profiles measured in LCT-B sanidine are growth profiles indicates that little time passed that would have allowed for observable diffusive relaxation.

We conclude that slow-path Mg diffusion is likely dominating the signal measured in LCT-B sanidine, which merits its use of slow-path diffusion and report a maximum timescale of a few decades. Fast-path diffusion operates simultaneously and while it is unlikely to be significantly contributing to the Mg signal measured in LCT-B sanidine, there is still potential that timescales as short as weeks can be captured by fast-path Mg diffusion, given appropriate analytical precision. Therefore, we bracket a final timescale between rejuvenation and eruption as short as weeks but no more than a few decades. As emphasized in prior work (Shamloo and Till, 2019), this underlines the importance of examining profiles of multiple elements with significantly different diffusivities to accurately constrain diffusion timescales in magmatic systems. Although we advocate that the Mg profiles observed in the LCT sanidine are dominated by slow-path diffusion, Mg fast-path diffusion may be identifiable for sanidine with Mg concentrations significantly greater than that of the several ppm in LCT. If so, we recommend assessment of the evidence for slow-path vs. fast-path diffusion and the use of both diffusion coefficients to bracket likely diffusion timescales.

5. SUMMARY & CONCLUSIONS

Mg diffusion experiments in volcanic sanidine with variable orthoclase contents (Or_{71} and Or_{82}) show no resolvable dependence on K/Na composition. Current data suggests that diffusion in sanidine is far more complex than previously recognized. Two modes of Mg diffusion operate simultaneously in sanidine evident by irregular depth profile shapes that do not conform to the standard analytical solution to the diffusion equation. A model was developed based on multi-site diffusion reactions of Mg in sanidine in order to better characterize measured depth profiles. The slow-path diffusion mechanism close to the crystal surface is likely rate-limited by the charge compensating reactions between framework elements such as Al and other abundant cations in sanidine such as Ba and Sr. Alternatively, fast-path Mg diffusion is three orders of magnitude faster than slow-path Mg diffusion and is comparable in rate and Arrhenius parameters to Mg diffusion in plagioclase. Fast-path diffusion likely operates by interstitial and vacancy site migration. We recommend when using these data for geospeedometry, to first quantify Ba and Sr distribution in the crystal of interest to assess which mode of diffusion is likely to dominate. It is also imperative to assess the relative importance of diffusion vs. growth in governing observed concentration profiles. For most analytical instruments at present, pure fast-path diffusion will likely not be detectable if there are low concentrations (several ppm) of Mg or too narrow zone of growth/diffusion in crystals. This study provides novel time estimates for magmatic rejuvenation that played a role in initiating the Lava Creek Tuff supereruption at Yellowstone Caldera as short as weeks but no more than a few decades. This study also demonstrates the complexity that may exist in experimentally-derived geospeedometers and the importance in applying them accurately to natural systems.

Declaration of Competing Interest

The authors declare that they have no known competing financial interests or personal relationships that could have appeared to influence the work reported in this paper.

ACKNOWLEDGEMENTS

A special thanks to Kevin Czaja at the Mineralogical and Geological Museum at Harvard and Jürgen Schreuer at Ruhr Universität Bochum for generously providing samples that made this study possible. This work was supported by the Geological Society of America's MGVP Student Research Grant Award to Shamloo and by a National Science Foundation CAREER grant [EAR-1654584] to Till. Analyses for these experiments were made possible by the NSF-funded [EAR- 1819550] SIMS-NanoSIMS facility at ASU and we acknowledge the use of facilities (including optical profilometer and electron microprobe) within the Eyring Materials Center at Arizona State University supported in part by NNCI-ECCS-1542160. Authors would like to provide a special thank you to Eli Bloch for extensive review, discussion, and providing code that greatly improved this manuscript. Additionally, thank you to Daniele Cherniak for thoughtful and constructive com-

ments. Lastly, thanks to James Van Orman, Kathi Faak, Ian Parsons, and Alyssa Anderson for insightful conversations along the way.

APPENDIX A. SUPPLEMENTARY MATERIAL

Supplementary data to this article can be found online at https://doi.org/10.1016/j.gca.2021.01.044.

REFERENCES

Allan A., Morgan D., Wilson C. and Millet M. A. (2013) From mush to eruption in centuries: assembly of the super-sized Oruanui magma body. *Contrib. Mineral. Petrol.* **166**, 143–164.

Almeev R. R., Bolte T., Nash B. P., Holtz F., Erdmann M. and Cathey H. E. (2012) High-temperature, low-H_2O silicic magmas of the Yellowstone hotspot: an experimental study of rhyolite from the Bruneau-Jarbidge Eruptive Center, Central Snake River Plain, USA. *J. Pet.* **53**, 1837–1866.

Anderson A. T., Davis A. M. and Lu F. (2000) Evolution of Bishop Tuff rhyolitic magma based on melt and magnetite inclusions and zoned phenocrysts. *J. Petrol.* **41**, 449–473.

Audétat A. (2013) Origin of Ti-rich rims in quartz phenocrysts from the Upper Bandelier Tuff and the Tunnel Spring Tuff, southwestern USA. *Chem. Geol.* **360**, 99–104.

Bachmann O., Deering C. D., Lipman P. W. and Plummer C. (2014) Building zoned ignimbrites by recycling silicic cumulates: Insight from the 1,000 km3 Carpenter Ridge Tuff, CO. *Contrib. Mineral. Petrol.* **167**, 1–13.

Behrens H., Johannes W. and Schmalzried H. (1990) On the mechanisms of cation diffusion processes in ternary feldspars. *Phys. Chem. Minerals* **17**, 62–78.

Beran A. (1986) A model of water allocation in alkali feldspar, derived from infrared-spectroscopic investigations. *Phys. Chem. Minerals* **13**, 306–310.

Bernotat-Wulf H., Bertelmann D. and Wondratschek H. (1988) The annealing behaviour of Eifel sanidine (Volkesfeld) III. The influence of the sample surface and sample size on the order-disorder transformation rate. *Neues Jahrbuch für Mineralogie Monatshefte* **11**, 503–515.

Bertelmann D., Walther J. and Wondratschek H. (1987) Annealing-induced inclusions and transformation behaviour of Eifel sanidines. *Terra Cognita* **7**, 257–258.

Bindeman I. N. and Valley J. W. (2001) Low-d18O rhyolites from Yellowstone: Magmatic evolution based on analyses of zircon and individual phenocrysts. *J. Petrol.* **42**, 1491–1517.

Bloch E., Ganguly J., Hervig R. and Cheng W. (2015) 176Lu–176Hf geochronology of garnet I: experimental determination of the diffusion kinetics of Lu3+ and Hf4+ in garnet, closure temperatures and geochronological implications. *Contrib. to Mineral. Petrol.* **169**, 12.

Bloch E. M., Jollands M. C., Devoir A., Bouvier A. S., Ibañez-Mejia M. and Baumgartner L. P. (2020) Multispecies diffusion of yttrium, rare earth elements and hafnium in garnet. *J. Pet.*.

Bolte T., Holtz F., Almeev R. and Nash B. (2015) The Blacktail Creek Tuff: an analytical and experimental study of rhyolites from the Heise volcanic field, Yellowstone hotspot system. *Cont. Mineral. Petrol.* **169**, 15.

Cashman K. V. and Sparks R. S. J. (2013) How volcanoes work: A 25 year perspective. *GSA Bull.* **664–690**.

Chamberlain K. J., Morgan D. J. and Wilson C. J. N. (2014) Timescales of mixing and mobilisation in the Bishop Tuff magma body: Perspectives from diffusion chronometry. *Contrib. Mineral. Petrol.* **168**, 1–24.

Cherniak D. J. and Watson E. B. (1992) A study of strontium diffusion in K-feldspar, Na-K feldspar and anorthite using Rutherford Backscattering Spectroscopy. *Earth Planet. Sci. Lett.* **113**, 411–425.

Cherniak D. J. and Watson E. B. (1994) A study of strontium diffusion in plagioclase using Rutherford backscattering spectroscopy. *Geochim. Cosmochim. Acta* **58**, 5179–5190.

Cherniak D. J. (1995) Diffusion of lead in plagioclase and K-feldspar: an investigation using Rutherford backscattering and resonant nuclear reaction analysis. *Contrib. Mineral. Petrol.* **120**, 358–371.

Cherniak D. J. (1996) Strontium diffusion in sanidine and albite, and general comments on strontium diffusion in alkali feldspars. *Geochim. Cosmochim. Acta* **60**, 5037–5043.

Cherniak D. J. (2002) Ba diffusion in feldspar. *Geochim. Cosmochim. Acta* **66**, 1641–1650.

Cherniak D. J. (2003) REE diffusion in feldspar. *Chem. Geol.* **193**, 25–41.

Cherniak D. J., Watson E. B. and Wark D. A. (2007) Ti diffusion in quartz. *Chem. Geol.* **236**, 65–74.

Cherniak D. J. (2010) Cation diffusion in feldspars. *Rev. Min. Geochem.* **72**, 691–733.

Christoffersen R., Yund R. A. and Tullis J. (1983) Inter-diffusion of K and Na in alkali feldspars; diffusion couple experiments. *Am. Min.* **68**, 1126–1133.

Christiansen R. L. (2001) The Quaternary and Pliocene Yellowstone Plateau volcanic field of Wyoming, Idaho, and Montana. *U.S. Geol. Surv. Prof. Pap.* **729**, 1–146.

Cooper K. M. and Kent A. J. R. (2014) Rapid remobilization of magmatic crystals kept in cold storage. *Nature* **506**, 480–483.

Costa F. and Chakraborty S. (2004) Decadal time gaps between mafic intrusion and silicic eruption obtained from chemical zoning patterns in olivine. *Earth Planet. Sci. Lett.* **227**, 517–530.

Costa F., Chakraborty S. and Dohmen R. (2003) Diffusion coupling between trace and major elements and a model for calculation of magma residence times using plagioclase. *Geochim. Cosmochim. Acta* **67**, 2189–2200.

Crank J. (1975) *The mathematics of diffusion*, 2nd end.

Dohmen R., Kasemann S. A., Coogan L. and Chakraborty S. (2010) Diffusion of Li in olivine. Part I: experimental observations and a multi species diffusion model. *Geochim. Cosmochim. Acta* **74**, 274–292.

Druitt T. H., Costa F., Deloule E., Dungan M. and Scaillet B. (2012) Decadal to monthly timescales of magma transfer and reservoir growth at a caldera volcano. *Nature* **482**, 77–80.

Faak K., Chakraborty S. and Coogan L. A. (2013) Mg in plagioclase: Experimental calibration of a new geothermometer and diffusion coefficients. *Geochim. Cosmochim. Acta* **123**, 95–217.

Foland K. A. (1974) Alkali diffusion in orthoclase. *Cheochem. Trans. Kin.* **634**, 77–98.

Giletti B. J. (1991) Rb and Sr diffusion in alkali feldspars, with implications for cooling histories of rocks. *Geochim. Cosmochim. Acta* **55**, 1331–1343.

Giletti B. J. and Casserly J. E. D. (1994) Strontium diffusion kinetics in plagioclase feldspars. *Geochim. Cosmochim. Acta* **58**, 3785–3793.

Giletti B. J. and Shanahan T. M. (1997) Alkali diffusion in plagioclase feldspar. *Chem. Geol.* **139**, 3–20.

Ginibre C., Wörner G. and Kronz A. (2004) Structure and dynamics of the Laacher See magma chamber (Eifel, Germany) from major and trace element zoning in sanidine: a cathodoluminescence and electron microprobe study. *J. Petrol.* **45**, 2197–2223.

Grove T. L., Baker M. B. and Kinzler R. J. (1984) Coupled CaAl-NaSi diffusion in plagioclase feldspar: Experiments and appli-

cations to cooling rate speedometry. *Geochim. Cosmochim. Acta* **48**, 2113–2121.
Gualda G. A. R. and Sutton S. R. (2016) The year leading to a supereruption. *PLoS ONE* **11**, 1–18.
Hervig R. L. and Dunbar N. W. (1992) Cause of chemical zoning in the Bishop (California) and Bandelier (New Mexico) magma chambers. *Earth Planet. Sci. Lett.* **111**, 97–108.
Hildreth W. and Wilson C. J. (2007) Compositional zoning of the Bishop Tuff. *J. Petrol.* **48**, 951–999.
Hofmeister A. M. and Rossman G. R. (1985) A model for the irradiative coloration of smokey feldspar and the inhibiting influence of water. *Phys. Chem. Minerals* **12**, 324–332.
Icenhower J. and London D. (1996) Experimental partitioning of Rb, Cs, Sr, and Ba between alkali feldspar and peraluminous melt. *Am. Min.* **81**, 719–734.
Jollands M. C., Kempf E., Hermann J. and Müntener O. (2019) Coupled inter-site reaction and diffusion: rapid dehydrogenation of silicon vacancies in natural olivine. *Geochim. Cosmochim. Acta* **262**, 220–242.
Jollands M. C., Bloch E. and Müntener O. (2020) New Ti-in-quartz diffusivities reconcile natural Ti zoning with time scales and temperatures of upper crustal magma reservoirs. *Geology* **48**, 654–657.
Landi P., La Felice S., Petrelli M., Vezzoli L. M. and Principe C. (2019) Deciphering textural and chemical zoning of K-feldspar megacrysts from Mt. Amiata Volcano (Southern Tuscany, Italy): Insights into the petrogenesis and abnormal crystal growth. *Lithos* **324**, 569–583.
Lasaga A. C. (1983) Geospeedometry: an extension of geothermometry. In *Kinetics and equilibrium in mineral reactions*. Springer, New York, NY, pp. 81–114.
LaTourrette T. and Wasserburg G. J. (1998) Mg diffusion in anorthite: implications for the formation of early solar system planetesimals. *Earth Planet. Sci. Lett.* **158**, 91–108.
Lehmann G. (1984) Spectroscopy of feldspars. In Feldspars and Feldspathoids: Structure, Properties, and Occurrences. *NATO Adv. Study Inst Springer, Dordrecht* **142**, 121–162.
Longhi J. and Hays J. F. (1979) Phase equilibria and solid solution along the join CaAl 2 Si 2 O 8-SiO 2. *Am. J. Sci.* **279**, 876–890.
Martin V. M., Morgan D. J., Jerram D. A., Caddick M. J., Prior D. J. and Davidson J. P. (2008) Bang! Month-scale eruption triggering at Santorini volcano. *Science* **321**, 1178-1178.
Matthews N. E., Huber C., Pyle D. M. and Smith V. C. (2012) Timescales of magma recharge and reactivation of large silicic systems from Ti diffusion in quartz. *J. Petrol.* **53**, 1385–1416.
Matthews N. E., Vazquez J. A. and Calvert A. T. (2015) Age of the L ava C reek supereruption and magma chamber assembly at Yellowstone based on 40 Ar/39 Ar and U-Pb dating of sanidine and zircon crystals. *Geochem., Geophys. Geosys.* **16**, 2508–2528.
Morgan D. J. and Blake S. (2006) Magmatic residence times of zoned phenocrysts: introduction and application of the binary element diffusion modelling (BEDM) technique. *Cont. Mineral. Petrol.* **151**, 58–70.
Morgan D. J., Blake S., Rogers N. W., De Vivo B., Rolandi G. and Davidson J. P. (2006) Magma chamber recharge at Vesuvius in the century prior to the eruption of A.D. 79. *Geology* **34**, 845–848. https://doi.org/10.1130/G22604.1.
Parsons I. and Brown W. L. (1991) Mechanisms and Kinetics of Exsolution—Structural Control of Diffusion and Phase Behavior in Alkali Feldspars Alkali Feldspars. In *Diffusion, Atomic Ordering, and Mass Transport*. Springer, New York, pp. 304–344.
Parsons I. and Lee M. R. (2005) Minerals are not just chemical compounds. *Can. Mineral.* **43**, 1959–1992.
Ren M. (2004) Partitioning of Sr, Ba, Rb, Y and LREE between alkali feldspar and peraluminous silicic magma. *Am. Mineral.* **89**, 1290–1303.
Rubin A. E., Cooper K. M., Till C. B., Kent A. J., Costa F., Bose M., Gravley D., Deering C. and Cole J. (2017) Rapid cooling and cold storage in a silicic magma reservoir recorded in individual crystals. *Science* **356**, 1154–1156.
Ruth D. C. S., Costa F. and de Maisonneuve C. B. (2018) Crystal and melt inclusion timescales reveal the evolution of magma migration before eruption. *Nat. Comm.* **9**, 2657.
Saunders K., Blundy J., Dohmen R. and Cashman K. (2012) Linking petrology and seismology at an active volcano. *Science* **336**, 1023–1027.
Shamloo H. I. and Till C. B. (2019) Decadal transition from quiescence to supereruption: petrologic investigation of the Lava Creek Tuff, Yellowstone Caldera, WY. *Contrib. Mineral. Petrol.* **174**, 32.
Shannon R. D. (1976) Revised effective ionic radii and systematic studies of interatomic distances in halides and chalcogenides. *Acta Crystal.* **32**, 751–767.
Stelten M. E., Cooper K. M., Vazquez J. A., Reid M. R., Barfod G. H., Wimpenny J. and Yin Q. Z. (2013) Magma mixing and the generation of isotopically juvenile silicic magma at Yellowstone caldera inferred from coupling 238 U–230 Th ages with trace elements and Hf and O isotopes in zircon and Pb isotopes in sanidine. *Contrib. Mineral. Petrol.* **166**, 587–613.
Stelten M. E., Cooper K. M., Wimpenny J. B., Vazquez J. A. and Yin Q. Z. (2017) The role of mantle-derived magmas in the isotopic evolution of Yellowstone's magmatic system. *Geochem. Geophys. Geosys.* **18**, 1350–1365. https://doi.org/10.1002/2016GC006664.
Szymanowski D., Ellis B. S., Wotzlaw J. and Bachmann O. (2019) Maturation and rejuvenation of a silicic magma reservoir: High-resolution chronology of the Kneeling Nun Tuff. *Earth Planet. Sci. Lett.* **510**, 103–115.
Till C. B., Vazquez J. A. and Boyce J. W. (2015) Months between rejuvenation and volcanic eruption at Yellowstone caldera, Wyoming. *Geology* **43**, 695–698.
Turner S. and Costa F. (2007) Measuring Timescales of Magmatic Evolution. *Elements* **3**, 267–272.
Van Orman J. A., Grove T. L. and Shimizu N. (2001) Rare earth element diffusion in diopside: influence of temperature, pressure, and ionic radius, and an elastic model for diffusion in silicates. *Contrib. Mineral. Petrol.* **141**, 687–703.
Van Orman J. A., Cherniak D. J. and Kita N. T. (2014) Magnesium diffusion in plagioclase: Dependence on composition, and implications for thermal resetting of the 26Al-26Mg early solar system chronometer. *Earth Planet. Sci. Lett.* **385**, 79–88.
van Zalinge M. E., Sparks R. S. J. and Blundy J. D. (2017) Petrogenesis of the large-volume Cardones Ignimbrite, Chile; Development and destabilization of a complex magma–mush system. *J. Petrol.* **58**, 1975–2006.
Yund R. A. (1984) Alkali feldspar exsolution: kinetics and dependence on alkali interdiffusion. In *Feldspars and Feldspathoids*. Springer, Dordrecht, pp. 281–315.
Yund R. A. (1986) Interdiffusion of NaSi-CaAl in peristerite. *Phys. Chem. Miner.* **13**, 11–16.
Zellmer G. F., Blake S., Vance D., Hawkesworth C. and Turner S. (1999) Plagioclase residence times at two island arc volcanoes (Kameni Islands, Santorini, and Soufriere, St. Vincent) determined by Sr diffusion systematics. *Contrib. Mineral. Petrol.* **136**, 345–357.
Zellmer G. F. and Clavero J. E. (2006) Using trace element correlation patterns to decipher a sanidine crystal growth chronology: an example from Taapaca volcano, Central Andes. *J. Volcanol. Geotherm. Res.* **156**, 291–301.

Associate editor: Wim van Westrenen